

**Chiral extrapolation of octet-baryon charge radii**P. Wang,<sup>1,2</sup> D. B. Leinweber,<sup>3</sup> A. W. Thomas,<sup>1,4</sup> and R. D. Young<sup>5</sup><sup>1</sup>*Jefferson Laboratory, 12000 Jefferson Avenue, Newport News, Virginia 23606 USA*<sup>2</sup>*Theoretical Physics Center for Science Facilities (TPCSF), CAS, P. R. China*<sup>3</sup>*Special Research Center for the Subatomic Structure of Matter (CSSM) and Department of Physics, University of Adelaide 5005, Australia*<sup>4</sup>*Department of Physics, College of William and Mary, Williamsburg, Virginia 23187 USA*<sup>5</sup>*Physics Division, Argonne National Laboratory, Argonne, Illinois 60439, USA*

(Received 6 October 2008; revised manuscript received 1 April 2009; published 1 May 2009)

The charge radii of octet-baryons obtained in quenched lattice-QCD calculations are extrapolated within heavy-baryon chiral perturbation theory. Finite-range regularization is applied to improve the convergence of the chiral expansion and to provide estimates of quenching artifacts. Lattice values of quark distribution radii and baryon charge radii for  $m_\pi^2$  in the range (0.1, 0.7) GeV<sup>2</sup> are described very well with finite-range regularization. Upon estimating corrections for both finite-volume and quenching effects, the obtained charge radii of the proton, neutron and  $\Sigma^-$  are in good agreement with experimental measurements. The predicted charge radii of the remaining octet-baryons have not yet been measured and present a challenge to future experiments.

DOI: 10.1103/PhysRevD.79.094001

PACS numbers: 13.40.-f, 11.10.Gh, 12.39.Fe, 14.20.-c

**I. INTRODUCTION**

The study of the electromagnetic form factors of baryons is of crucial importance to understanding the non-perturbative properties of QCD. Though QCD is accepted as the fundamental theory of the strong interaction, it remains a theoretical challenge to quantitatively probe the nonperturbative domain. There are many effective methods and phenomenological models that have been applied to study the electromagnetic properties of baryons: the cloudy bag model [1], the constituent-quark model [2,3], the  $1/N_c$  expansion approach [4], the perturbative chiral quark model [5], the extended vector meson dominance model [6], the quark-diquark model [7], and the Schwinger-Dyson formalism [8–10]. Various formulations of heavy-baryon chiral perturbation theory ( $\chi$ PT) have also been widely applied to this problem [11–14]. It has been observed that expansions in  $\chi$ PT are consistent with experimental results up to  $Q^2 \simeq 0.1$  GeV<sup>2</sup> [12]. Extensions of  $\chi$ PT to explicitly incorporate vector mesons have been demonstrated to improve the applicability to  $Q^2 \simeq 0.4$  GeV<sup>2</sup> [15].

As well as the above model calculations, the past few years have seen increased activity in lattice-QCD studies of the electromagnetic form factors. Significant efforts to probe baryon electromagnetic structure in lattice QCD have been driven by the Adelaide group [16,17], the Cyprus group [18], and the QCDSF [19–21] and LHP Collaborations [22,23]. While lattice QCD provides the strongest tool for studying nonperturbative phenomena in QCD, it does come with its own challenges. In particular, artifacts of (unitary) lattice simulations arising from discretization, finite-volume, and unphysical quark masses all need to be carefully dealt with to extract the predictions of QCD relevant to the real world. (There are further, more

complicated issues in dealing with nonunitary approximations: partial- and full-quenching, 4th rooting, mixed-action etc.).

The principle focus of this manuscript is on the quark-mass dependence of baryon charge radii and the chiral extrapolation of lattice simulation results performed at unphysically large quark masses. Characterizing the quark-mass dependence of hadronic observables in QCD can be achieved within the low-energy effective theory of QCD,  $\chi$ PT—see, for example, Bernard’s recent review on baryon phenomena [24].

A celebrated feature of such effective theories is the model independence of leading nonanalytic contributions to quark-mass expansions [25]. Such *chiral logs* are a direct consequence of the spontaneously broken chiral symmetry of QCD. Neglecting such behavior in chiral extrapolations (of even high-quality lattice calculations) can potentially render results that have less resemblance of QCD than some of the models discussed above. While the inclusion of such logs in chiral extrapolations is necessary to maintain QCD in the extraction of physical results [26–30], this can be a challenging task because of the poor convergence properties of the effective field theory (EFT) expansion at moderate quark masses [31–34].

In this manuscript we work with finite-range regularization (FRR) to improve the convergence properties of the quark-mass expansion of the EFT [31,32,35].

As an effective theory describing long-distance phenomena,  $\chi$ PT can also describe the finite-volume effects of restricting the underlying theory to finite boundary conditions [36]. The accuracy of these corrections is also subject to the usual conditions, being at light-enough quark masses and large-enough volumes. In this work we impose the finite boundary conditions on the relevant one-loop

graphs. These provide the leading estimates of the finite-volume corrections.

The lattice simulation results studied in this paper come from the CSSM Lattice Collaboration [17]. These lattice results have been evaluated with quenched gauge-field ensembles. With the underlying dynamics modified by neglecting the quark loops of the QCD vacuum, the effective low-energy theory is described by quenched  $\chi$ PT ( $Q\chi$ PT). For baryons, this was first formulated by Labrenz and Sharpe [37] and for relevant work on the electromagnetic form factors in quenched and partially quenched theories see Refs. [38–41].

Given quenched lattice results, we use the leading meson-loop diagrams to estimate the corrections in going to the fully dynamical theory [32]. This is based on the empirical observation that the discrepancies between the quenched and dynamical nucleon and Delta-baryon masses are well described by the associated leading meson-loop dressings, as evaluated with a dipole finite-range regulator [42]. The physical picture drawn from these results is quite intuitive, once the interquark forces are matched at an intermediate distance scale (in this case, the Sommer scale [43]) the differing long-range features are dominantly described by the low-energy EFT. In this case the FRR scale acts to separate the long from the short. Further, any residual difference in the  $q\bar{q}$  force at quite short distances does not appear to play a significant role in the bulk, low-energy structure.

In Sec. II, we will briefly introduce the chiral Lagrangian, which is used for the octet charge form factors. Charge form factors and radii are calculated in Sec. III with quenched and full-QCD. Numerical results are presented in Sec. IV, and finally Sec. V is the summary.

## II. CHIRAL LAGRANGIAN

There are many papers that deal with heavy-baryon chiral perturbation theory. For details see, for example, Refs. [24,44,45]. For completeness, we briefly introduce the formalism in this section. In heavy-baryon chiral perturbation theory, the lowest chiral Lagrangian for the baryon-meson interaction, which will be used in the calculation of the octet-baryon charge form factors, is

$$\begin{aligned} \mathcal{L}_v = & i \text{Tr} \bar{B}_v (\mathbf{v} \cdot \mathcal{D}) B_v + 2D \text{Tr} \bar{B}_v S_v^\mu \{A_\mu, B_v\} \\ & + 2F \text{Tr} \bar{B}_v S_v^\mu [A_\mu, B_v] - i \bar{T}_v^\mu (\mathbf{v} \cdot \mathcal{D}) T_{v\mu} \\ & + \mathcal{C} (\bar{T}_v^\mu A_\mu B_v + \bar{B}_v A_\mu T_v^\mu), \end{aligned} \quad (1)$$

where  $S_\mu$  is the covariant spin-operator defined as

$$S_v^\mu = \frac{i}{2} \gamma^5 \sigma^{\mu\nu} v_\nu. \quad (2)$$

Here,  $v^\nu$  is the nucleon four velocity [in the rest frame, we have  $v^\nu = (1, \vec{0})$ ]. We incorporate the explicit propagation of octet and decuplet baryon states, with  $D$ ,  $F$ , and  $\mathcal{C}$  denoting the relevant meson-baryon couplings (which, in

principle, are to be determined in the chiral limit). The chiral covariant derivative  $D_\mu$  is written as  $D_\mu B_v = \partial_\mu B_v + [V_\mu, B_v]$ . The pseudoscalar meson octet couples to the baryon field through the vector and axial vector combinations

$$V_\mu = \frac{1}{2} (\zeta \partial_\mu \zeta^\dagger + \zeta^\dagger \partial_\mu \zeta), \quad A_\mu = \frac{1}{2} (\zeta \partial_\mu \zeta^\dagger - \zeta^\dagger \partial_\mu \zeta), \quad (3)$$

where

$$\zeta = e^{i\phi/f}, \quad f = 93 \text{ MeV}. \quad (4)$$

The matrix of pseudoscalar fields  $\phi$  is expressed as

$$\phi = \frac{1}{\sqrt{2}} \begin{pmatrix} \frac{1}{\sqrt{2}} \pi^0 + \frac{1}{\sqrt{6}} \eta & \pi^+ & K^+ \\ \pi^- & -\frac{1}{\sqrt{2}} \pi^0 + \frac{1}{\sqrt{6}} \eta & K^0 \\ K^- & \bar{K}^0 & -\frac{2}{\sqrt{6}} \eta \end{pmatrix}. \quad (5)$$

$B_v$  and  $T_v^\mu$  are velocity-dependent fields, which are related to the original baryon octet and decuplet fields  $B$  and  $T^\mu$  by

$$B_v(x) = e^{im_N \not{v} x^\mu} B(x), \quad (6)$$

$$T_v^\mu(x) = e^{im_N \not{v} x^\mu} T^\mu(x). \quad (7)$$

In the chiral  $SU(3)$  limit, the octet baryons are degenerate. As the physical strange-quark mass is significant, we incorporate the physical mass splittings in the evaluation of the chiral-loop diagrams.

The explicit form of the octet-baryon matrix is written as

$$B = \begin{pmatrix} \frac{1}{\sqrt{2}} \Sigma^0 + \frac{1}{\sqrt{6}} \Lambda & \Sigma^+ & p \\ \Sigma^- & -\frac{1}{\sqrt{2}} \Sigma^0 + \frac{1}{\sqrt{6}} \Lambda & n \\ \Xi^- & \Xi^0 & -\frac{2}{\sqrt{6}} \Lambda \end{pmatrix}. \quad (8)$$

The baryon decuplets are defined by the rank-3 symmetric tensor, with unique elements given by

$$\begin{aligned} T_{111} &= \Delta^{++}, & T_{112} &= \frac{1}{\sqrt{3}} \Delta^+, \\ T_{122} &= \frac{1}{\sqrt{3}} \Delta^0, & T_{222} &= \Delta^-, \\ T_{113} &= \frac{1}{\sqrt{3}} \Sigma^{*+}, & T_{123} &= \frac{1}{\sqrt{6}} \Sigma^{*0}, \\ T_{223} &= \frac{1}{\sqrt{3}} \Sigma^{*-}, & T_{133} &= \frac{1}{\sqrt{3}} \Xi^{*0}, \\ T_{233} &= \frac{1}{\sqrt{3}} \Xi^{*-}, & T_{333} &= \Omega^-. \end{aligned} \quad (9)$$

In the heavy-baryon formalism, the propagators of the octet and decuplet baryon,  $j$ , are, respectively, expressed as

$$\frac{i}{v \cdot k - \Delta^{jB} + i\varepsilon} \quad \text{and} \quad \frac{iP^{\mu\nu}}{v \cdot k - \Delta^{jB} + i\varepsilon}, \quad (10)$$

with  $P^{\mu\nu} = v^\mu v^\nu - g^{\mu\nu} - (4/3)S_v^\mu S_v^\nu$ .  $\Delta^{ab} = m_b - m_a$  is the mass difference of between the two baryons. The propagator of meson  $k$ , ( $k = \pi, K, \eta$ ) is the usual free propagator, i.e.

$$\frac{i}{k^2 - m_k^2 + i\epsilon}. \quad (11)$$

### III. CHARGE FORM FACTORS AND RADII

In the heavy-baryon formalism, the baryon form factors are defined as

$$\begin{aligned} \langle B(p') | J_\mu | B(p) \rangle = & \bar{u}(p') \left\{ v_\mu G_E(Q^2) \right. \\ & \left. + \frac{i\epsilon_{\mu\nu\alpha\beta} v^\alpha S_v^\beta q^\nu}{m_N} G_M(Q^2) \right\} u(p), \end{aligned} \quad (12)$$

where  $q = p' - p$  and  $Q^2 = -q^2$ . In this paper, we focus on the charge form factors, since we will extrapolate octet-baryon charge radii.

With the Lagrangian, the diagrams for the charge form factors are shown in Fig. 1. Our counting is ordered in terms of powers of the quark mass contributing to the given electric radii. For the purposes of counting, where the typical baryon mass splitting is small relative to the lattice meson masses, we treat the power of the quark mass that defines the order of a given diagram by neglecting the mass splitting,  $\Delta$ . The diagrams are nevertheless evaluated with the splittings restored. In the limit  $m_\pi \ll \Delta$ , diagrams a with the intermediate nucleon state and c give rise to the leading-log divergence of charge radii in full QCD. Diagram b gives a next to leading order nonanalytic term associated with the mass difference between octet and decuplet baryons. For the intermediate hyperon states of diagram a, the mass difference between hyperons and nucleon also provides a next to leading order nonanalytic term as diagram b. In this limit, we only have a partial

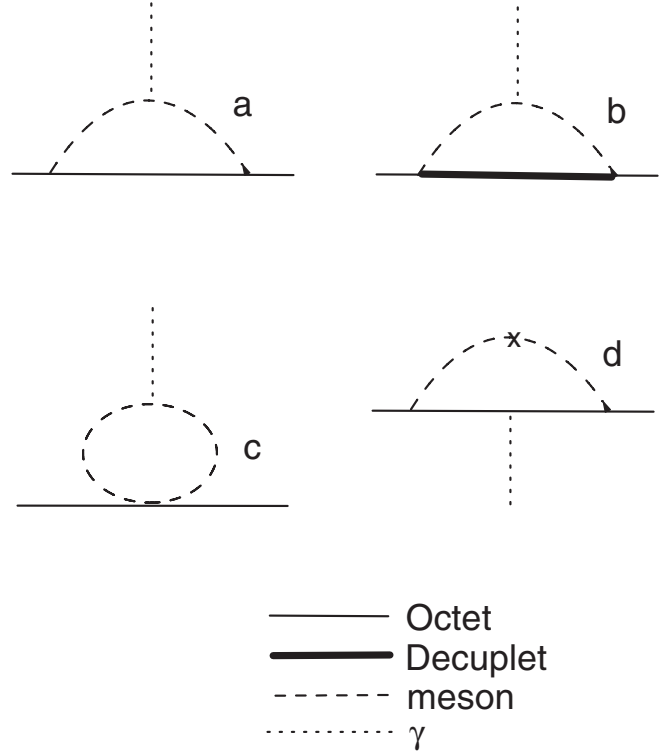


FIG. 1. Leading and next to leading order diagrams for the baryon charge form factors. Diagram d contributes only in the quenched case.

contribution of next order. This is certainly one of the places where our analysis is somewhat phenomenological. In the quenched case, each diagram has a different coefficient from that of dynamical QCD. In particular, diagram c has no contribution in the quenched case. Further, the double-hairpin diagram d contributes only in the quenched case, where the  $\eta'$  is degenerate with the pion.

Upon integration over  $k_0$ , the contribution to charge form factors of Fig. 1(a) can be expressed as

$$G_E^{(a)}(Q^2) = \frac{\beta_E^a}{16\pi^3 f_\pi^2} \int d\vec{k} \frac{u(\vec{k})u(\vec{k}-\vec{q})\vec{k} \cdot (\vec{k}-\vec{q})}{\omega(\vec{k})\omega(\vec{k}-\vec{q})(\omega(\vec{k}) + \omega(\vec{k}-\vec{q}))}. \quad (13)$$

Here,  $\omega(\vec{k}) = \sqrt{m^2 + \vec{k}^2}$  is the energy of the meson. We note that a summation over the relevant intermediate states is assumed. In our calculation we use the finite-range regularization and  $u(\vec{k})$  is the ultraviolet regulator. Both pion and kaon loops are included in the calculation. In the kaon case, Eq. (13) must of course, include the mass differences in the intermediate states. In full QCD, the coefficients are determined from the Lagrangian. In the quenched case, the coefficients are obtained as in Ref. [39]

using the quark flows of Figs. 2 and 3. The results are the same as those extracted within the graded symmetry formalism. In Fig. 3, the diagrams with  $\pi^0$  loop are not shown, since they have no contribution in the quenched or full QCD. They do contribute to the full-QCD valence sector and are included in our calculation for the valence sector results.

The contribution to the charge form factors of Fig. 1(b) can be written as

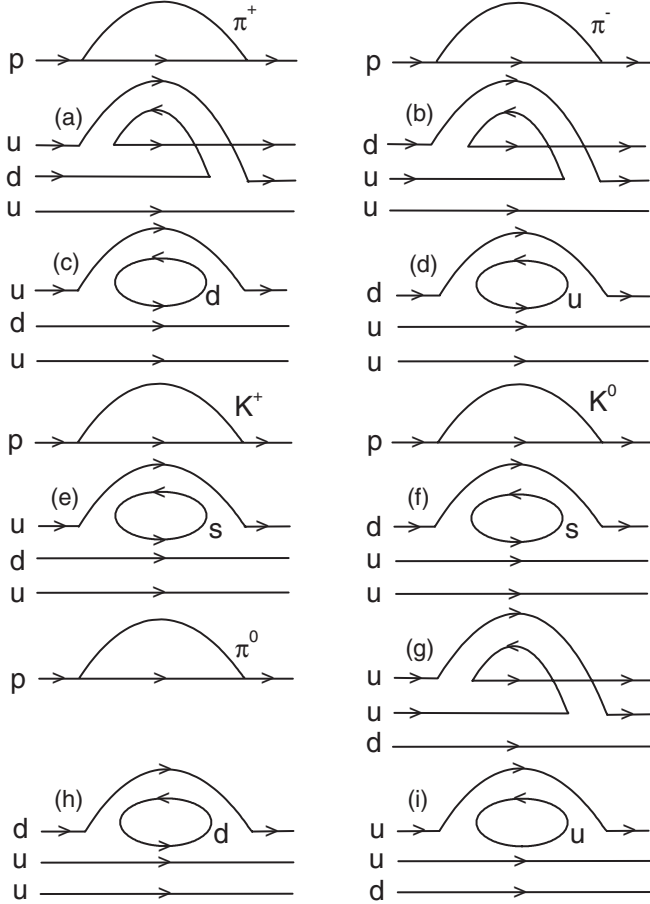


FIG. 2. Feynman diagrams of Fig. 1(a) for the proton, in terms of quark lines.

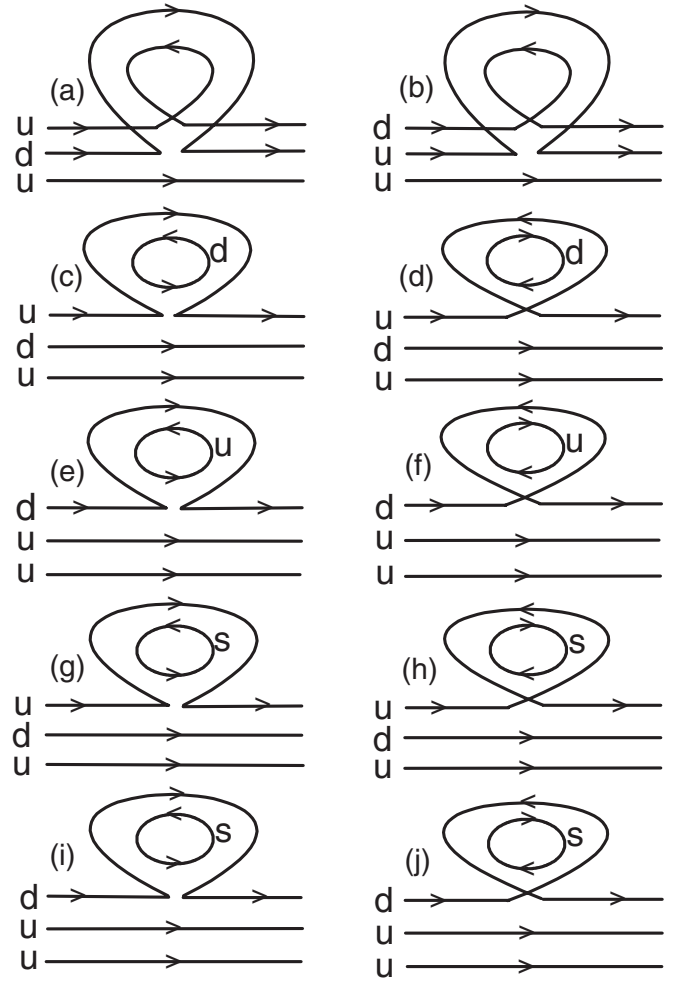


FIG. 3. Feynman diagrams of Fig. 1(c) for the proton, in terms of quark lines.

$$G_E^{(b)}(Q^2) = \frac{\beta_E^b}{16\pi^3 f_\pi^2} \int d\vec{k} \frac{u(\vec{k})u(\vec{k}-\vec{q})\vec{k}\cdot(\vec{k}-\vec{q})}{(\omega(\vec{k})+\Delta)(\omega(\vec{k}-\vec{q})+\Delta)(\omega(\vec{k})+\omega(\vec{k}-\vec{q}))}, \quad (14)$$

where  $\Delta$  is the positive mass difference between octet and decuplet baryons. The contribution to the form factors of Fig. 1(c) is expressed as

$$G_E^{(c)}(Q^2) = \frac{\beta_E^c}{16\pi^3 f_\pi^2} \int d\vec{k} \frac{u(\vec{k})^2}{\omega(\vec{k}+\vec{q}/2)+\omega(\vec{k}-\vec{q}/2)}. \quad (15)$$

In the above equations,  $\beta_E^i$  depends on the baryon type (or quark type), meson-loop type, and quenched or full QCD in the calculation.

In the quenched case, the double-hairpin term from the  $\eta'$  is expressed as

$$G_E^{(d)}(Q^2) = \frac{(3F-D)^2 M_0^2 G_E(Q^2)}{96\pi^3 f_\pi^2} \int d\vec{k} \frac{\vec{k}^2 u(\vec{k})^2}{\omega(\vec{k})^5} \equiv G_E(Q^2) G_E^d, \quad (16)$$

where  $M_0$  is the double-hairpin interaction strength. As a vertex renormalization in the heavy-baryon limit, the  $Q^2$  dependence factorizes to define a  $Q^2$ -independent  $G_E^d$ . We should mention that at the lowest order, the double-hairpin diagram is  $Q^2$  independent. The higher-order terms arising from the  $Q^2$  dependence of the contributions of this graph at the masses probed in the lattice simulations are negligible.

In the above formulas, the coefficients in quenched and full QCD can be obtained following the methodology of Ref. [39]. For example, the diagram Fig. 1(a) is shown in detail with quark lines in Fig. 2. For the pion loop, in full

TABLE I. Coefficient of proportionality for each diagram of Fig. 2 for the proton.

(a)	(b)	(c)(e)(i)	(d)(f)(h)	(g)
$(D + F)^2 - \frac{2}{3}D^2 - 2F^2$	$-(D - F)^2$	$\frac{2}{3}D^2 + 2F^2$	$(D - F)^2$	$\frac{1}{2}(D + F)^2 - \frac{5}{3}D^2 - 3F^2 + 2DF$

TABLE II. Coefficient of proportionality for each diagram of Fig. 3 for the proton.

(a)	(b)	(c)(g)	(d)(h)	(e)(i)	(f)(j)
0	0	2	-2	1	-1

QCD Figs. 2(a) and 2(c) make contributions, while in the quenched case Figs. 2(a) and 2(b) make contributions. Therefore, we need to get the coefficient for each diagram. The coefficient for Fig. 2(c) is the same as Fig. 2(e), which is known from the Lagrangian, since QCD is flavor blind. By subtracting this known coefficient from the total coefficient of full QCD, we can get the quenched one of Fig. 2(a). As an example, the coefficient of each diagram of Fig. 2 is listed in Table I. In the same way, the diagram of Fig. 1(c) can be shown in detail in Fig. 3. Table II gives the coefficient of each diagram of Fig. 3 for the proton. We can see that the coefficients for the first two diagrams Figs. 3(a) and 3(b) are zero, which means Fig. 1(c) has no contribution to the proton charge form factor in the quenched case. In fact, for other octet baryons, this diagram has no contribution either in the quenched case.

One can also concentrate on each quark contribution to the form factors. All the coefficients for each quark are shown in Tables III, IV, V, VI, VII, and VIII. In these Tables, only three baryons are listed. The coefficients for

neutron,  $\Sigma^-$ ,  $\Sigma^0$ ,  $\Xi^-$ , and  $\Lambda$  can be obtained by the following charge-symmetry relations:

$$u_n = d_p, \quad d_n = u_p, \quad s_n = s_p, \quad (17)$$

$$u_{\Sigma^-} = d_{\Sigma^+}, \quad d_{\Sigma^-} = u_{\Sigma^+}, \quad s_{\Sigma^-} = s_{\Sigma^+}, \quad (18)$$

$$u_{\Xi^-} = d_{\Xi^0}, \quad d_{\Xi^-} = u_{\Xi^0}, \quad s_{\Xi^-} = s_{\Xi^0}, \quad (19)$$

$$u_{\Sigma^0} = \frac{1}{2}(u_n + u_{\Xi^0}), \quad d_{\Sigma^0} = \frac{1}{2}(d_p + d_{\Xi^-}), \quad (20)$$

$$s_{\Sigma^0} = \frac{1}{2}(s_{\Sigma^+} + s_{\Sigma^-}),$$

$$u_{\Lambda} = d_{\Lambda} = \frac{1}{3} \left[ u_p + d_p + u_{\Xi^0} + d_{\Xi^0} - \frac{1}{2}(u_{\Sigma^+} + d_{\Sigma^-}) \right],$$

$$s_{\Lambda} = \frac{1}{3}(2s_p + 2s_{\Xi^0} - s_{\Sigma^+}). \quad (21)$$

We express our charge form factors as

$$G_E(Q^2) = Z - \frac{1}{6}(a_0 + a_2 m_\pi^2 + a_4 m_\pi^4) Q^2 + \sum_{i=a}^d G_E^{(i)}(Q^2), \quad (22)$$

where  $Z$  is the wave function renormalization constant of charge expressed as  $Z = G_E(Q^2 = 0) - \sum_{i=a}^d G_E^{(i)}(Q^2 = 0)$ .  $G_E(Q^2 = 0)$  is the charge of the baryon.  $G_E^{(i)}$  is expressed in Eqs. (13)–(16). Therefore,  $G_E(Q^2)$  can be written as

TABLE III. Coefficients  $\beta_E^a$  for quarks in the octet baryons in full and quenched QCD for Fig. 1(a). The intermediate meson is  $\pi$ .

Baryon\quark	QQCD			FQCD		
	$u$	$d$	$s$	$u$	$d$	$s$
$p$	$\frac{4}{3}D^2$	$-\frac{4}{3}D^2$	0	$(D + F)^2$	$-(D + F)^2$	0
$\Sigma^+$	0	0	0	$\frac{2}{3}D^2 \Lambda \pi$	$-\frac{2}{3}D^2 \Lambda \pi$	0
$\Xi^0$	0	0	0	$2F^2 \Sigma \pi$	$-2F^2 \Sigma \pi$	0
				$(D - F)^2$	$-(D - F)^2$	0

TABLE IV. Coefficients  $\beta_E^a$  for quarks in the octet-baryons in full and quenched QCD for Fig. 1(a). The intermediate meson is  $K$ .

Baryon\quark	QQCD			FQCD		
	$u$	$d$	$s$	$u$	$d$	$s$
$p$	0	0	0	$\frac{1}{6}(3F + D)^2 \Lambda K$	$(D - F)^2$	$-\frac{1}{6}(3F + D)^2 \Lambda K$
$\Sigma^+$	$\frac{1}{3}D^2 - F^2 + 2DF \Xi K$	0	$-\frac{1}{3}D^2 + F^2 - 2DF \Xi$	$\frac{1}{2}(D - F)^2 \Sigma K$	$-(D - F)^2$	$-\frac{3}{2}(D - F)^2 \Sigma K$
$\Xi^0$	$(D - F)^2 NK$	0	$-\frac{1}{3}D^2 + F^2 - 2DF \Xi$	$(D + F)^2$	$-(D - F)^2$	$(D - F)^2 NK$
	$-\frac{1}{2}(D + F)^2$	0	$\frac{1}{2}(D + F)^2$	$-(D + F)^2$	$-\frac{1}{6}(3F - D)^2 \Lambda K$	$\frac{1}{6}(3F - D)^2 \Lambda K$
	$+\frac{1}{6}(3F - D)^2 \Sigma K$	0	$-\frac{1}{6}(3F - D)^2 \Sigma K$	$-(D + F)^2$	$-\frac{1}{2}(D + F)^2 \Sigma K$	$-\frac{3}{2}(D + F)^2 \Sigma K$
	$-(D - F)^2 \Omega K$	0	$(D - F)^2 \Omega K$			

TABLE V. Coefficients  $\beta_E^b$  for quarks in the octet baryons in full and quenched QCD for Fig. 1(b). The intermediate meson is  $\pi$ .

Baryon\quark	QQCD			FQCD		
	$u$	$d$	$s$	$u$	$d$	$s$
$p$	$-\frac{1}{3}\mathcal{C}^2$	$\frac{1}{3}\mathcal{C}^2$	0	$-\frac{4}{9}\mathcal{C}^2$	$\frac{4}{9}\mathcal{C}^2$	0
$\Sigma^+$	0	0	0	$\frac{1}{9}\mathcal{C}^2$	$-\frac{1}{9}\mathcal{C}^2$	0
$\Xi^0$	0	0	0	$\frac{2}{9}\mathcal{C}^2$	$-\frac{2}{9}\mathcal{C}^2$	0

TABLE VI. Coefficients  $\beta_E^b$  for quarks in the octet baryons in full and quenched QCD for Fig. 1(b). The intermediate meson is  $K$ .

Baryon\quark	QQCD			FQCD		
	$u$	$d$	$s$	$u$	$d$	$s$
$p$	0	0	0	$\frac{1}{9}\mathcal{C}^2$	$\frac{2}{9}\mathcal{C}^2$	$-\frac{1}{3}\mathcal{C}^2$
$\Sigma^+$	$-\frac{4}{9}\mathcal{C}^2\Delta K$	$\frac{1}{9}\mathcal{C}^2\Xi^*K$	0	$\frac{4}{9}\mathcal{C}^2\Delta K$	$-\frac{1}{9}\mathcal{C}^2\Xi^*K$	$-\frac{2}{9}\mathcal{C}^2\Delta K$
$\Xi^0$	$-\frac{1}{9}\mathcal{C}^2\Sigma^*K$	$\frac{4}{9}\mathcal{C}^2\Omega K$	0	$\frac{1}{9}\mathcal{C}^2\Sigma^*K$	$-\frac{4}{9}\mathcal{C}^2\Omega K$	$-\frac{8}{9}\mathcal{C}^2\Delta K$

TABLE VII. Coefficients  $\beta_E^c$  for quarks in the octet baryons in full and quenched QCD for Fig. 1(c). The intermediate meson is  $\pi$ .

Baryon\quark	QQCD			FQCD		
	$u$	$d$	$s$	$u$	$d$	$s$
$p$	0	0	0	1	-1	0
$\Sigma^+$	0	0	0	2	-2	0
$\Xi^0$	0	0	0	1	-1	0

TABLE VIII. Coefficients  $\beta_E^c$  for quarks in the octet baryons in full and quenched QCD for Fig. 1(c). The intermediate meson is  $K$ .

Baryon\quark	QQCD			FQCD		
	$u$	$d$	$s$	$u$	$d$	$s$
$p$	0	0	0	2	1	-3
$\Sigma^+$	0	0	0	1	-1	0
$\Xi^0$	0	0	0	-1	-2	3

$$\begin{aligned}
G_E(Q^2) &= (G_E(Q^2 = 0) - \sum_{i=a}^d G_E^{(i)}(Q^2 = 0)) \\
&\quad - \frac{1}{6}(a_0 + a_2 m_\pi^2 + a_4 m_\pi^4)Q^2 + G_E^{(a)}(Q^2) \\
&\quad + G_E^{(b)}(Q^2) + G_E^{(c)}(Q^2)/(1 - G_E^d). \quad (23)
\end{aligned}$$

The above free parameters  $a_0$ ,  $a_2$ , and  $a_4$  are to be determined by fitting quenched lattice results with the described quenched loop integrals. The octet charge radii was inves-

igated in Refs. [13,47], where the  $SU(3)$  symmetry was applied. Our approach is based on an  $SU(2)$  framework where the strange-quark mass is held fixed, and the light

in anticipation of considering charge radii, we have defined the contribution from the double-hairpin, Fig. 1(d), to be proportional to the renormalized form factor using the factorization defined in Eq. (16). This follows a similar procedure to that outlined in Ref. [32].

The expansion in  $a_i$  characterizes the nonchiral quark-mass dependence of the electric charge radius of each baryon. To the leading order we work in this manuscript,  $a_0$  acts as a counterterm to the loops and thereby removing scale dependence of the formal expansion. Previous works have shown that including a partial contribution from the next higher analytic order beyond which one is working (e.g. Refs. [31,46]) can reduce the dependence on the regularization, motivating the  $a_2$  parameter. We have also included  $a_4$ , which has simply been included to better describe the lattice data, such that its justification is purely empirical (and not mathematical). Its presence mirrors the success obtained with a similar approach for the octet-baryon magnetic moments. Thereby our form should only be seen to incorporate the leading-logarithmic behavior of the EFT with the associated counterterm.

The Sachs charge radius is defined by

$$\langle r^2 \rangle_E = -6 \frac{dG_E(Q^2)}{dQ^2} \Big|_{Q^2=0}. \quad (24)$$

From the expression of  $G_E(Q^2)$ ,  $\langle r^2 \rangle_E$  can be written as

$$\langle r^2 \rangle_E = \left( a_0 + a_2 m_\pi^2 + a_4 m_\pi^4 - 6 \frac{d(G_E^{(a)}(Q^2) + G_E^{(b)}(Q^2) + G_E^{(c)}(Q^2))}{dQ^2} \Big|_{Q^2=0} \right) / (1 - G_E^d). \quad (25)$$

igated in Refs. [13,47], where the  $SU(3)$  symmetry was applied. Our approach is based on an  $SU(2)$  framework where the strange-quark mass is held fixed, and the light

quarks are always degenerate. Thereby each baryon isospin multiplet will carry independent low energy constants. Effectively, there will be two (independent)  $a_i$  for each multiplet. We do not impose the symmetry breaking patterns of  $SU(3)$ , as we regard the strange-quark mass as a scale that cannot be described well by this low-order expansion. We note it could be interesting to compare our effective  $SU(2)$  low energy constants with those extracted from earlier studies. We do not do this, but we have now included a comparison of the predictions for the radii of the physical states. In Ref. [48], the authors have developed two-flavor  $\chi$ PT to describe hyperons, which are embedded into  $SU(2)$  multiplets.

#### IV. NUMERICAL RESULTS

In the numerical calculations, the parameters are chosen as  $D = 0.76$  and  $F = 0.50$  ( $g_A = D + F = 1.26$ ). The coupling constant  $\mathcal{C}$  is chosen to be  $-2D$ , as estimated by  $SU(6)$  relations—which gives a similar value to that obtained from the hadronic decay width of the  $\Delta$ .

Here, the finite-range regulator is chosen to take the dipole form

$$u(k) = \frac{1}{(1 + k^2/\Lambda^2)^2}, \quad (26)$$

with  $\Lambda = 0.8 \pm 0.1$  GeV. This selected range of  $\Lambda$  for the dipole has been found to give good quantitative estimates of quenching artifacts for baryon masses [42] and magnetic moments [49].

Using a fixed strange-quark mass, we estimate the  $K$ -meson mass to obey the relationship

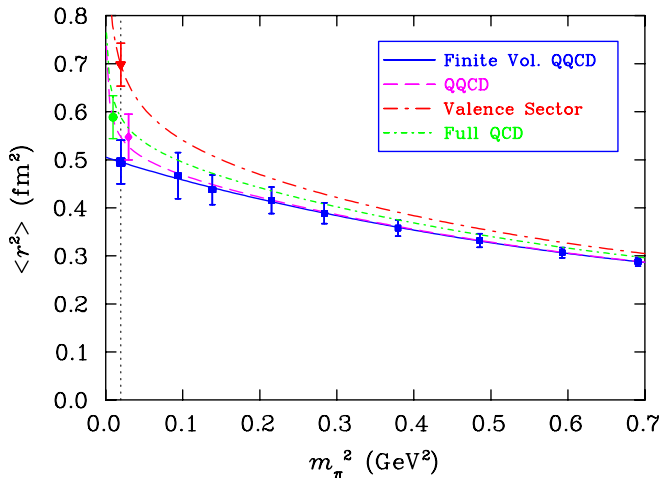


FIG. 4 (color online). The contribution of a single  $u$  quark with unit charge to the proton charge radius versus pion mass. The square, rhombus, triangle, and round symbols are for the finite-volume quenched QCD, infinite volume quenched QCD, valence sector and full-QCD results, respectively.

$$m_K^2 = \frac{1}{2}m_\pi^2 + m_K^2|_{\text{phy}} - \frac{1}{2}m_\pi^2|_{\text{phy}}. \quad (27)$$

We first study the  $u$ -quark contribution to the proton charge radius. Four kinds of extrapolations are shown in Fig. 4. The square, rhombus, triangle, and round symbols are for the finite-volume quenched QCD, infinite volume quenched QCD, valence sector, and full-QCD results, respectively. We remind the reader that the “valence” result denotes the connected current insertions in full QCD. The quenched lattice results are described very well. For infinite volume, all of them have log-divergent behavior at  $m_\pi = 0$ , which means that the pion cloud extends to infinity for a massless pion. For finite volume, the integration is replaced by the summation of the momentum, which shows no log divergence in the chiral limit. Technically, one should be cautious when considering the finite-volume curve in the domain where  $m_\pi L$  becomes small. Ideally, one would like to stay in the regime of  $m_\pi L > 6$  (or  $2\pi$ ). Ambitious lattice calculations push this down to 4 or 3, at which point one may be approaching the limits of describing the finite-volume corrections by the one-loop EFT. This limit, for our 2.56 fm box, is at pion masses of order 250 to 300 MeV, the lightest pion mass considered in the lattice simulations. This is not of serious concern, as *corrections* are performed at finite volume and *extrapolations* subsequently performed at infinite volume.

Figure 5 displays the  $d$ -quark contribution to the proton charge radius. The lines with different types have the same meaning as in Fig. 4. For infinite volume, the charge radius bends down as  $m_\pi$  approaches zero, indicating that the  $\bar{d}$  contributes more strongly to the long-ranging tail than the  $d$  in accord with the predominant  $p \rightarrow n\pi$  channel. At  $m_\pi = 0$ , the curves also have log-divergent behavior. We note that the positive charge radius is much like a

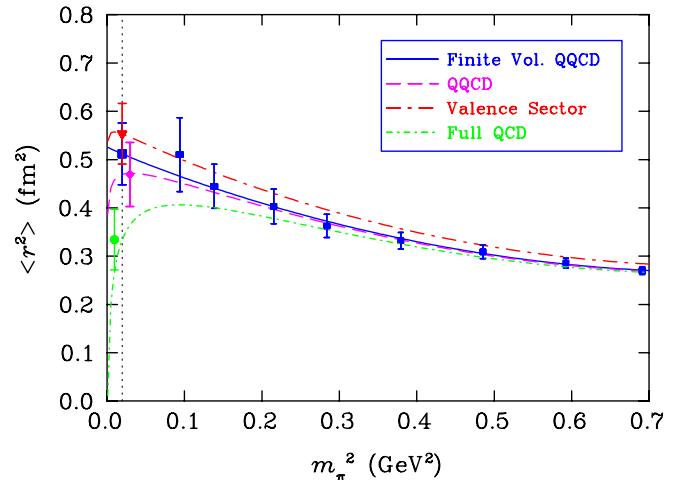


FIG. 5 (color online). The contribution of a  $d$  quark with unit charge to the proton charge radius versus pion mass. The square, rhombus, triangle, and round symbols are for the finite-volume quenched QCD, infinite volume quenched QCD, valence sector, and full-QCD results, respectively.

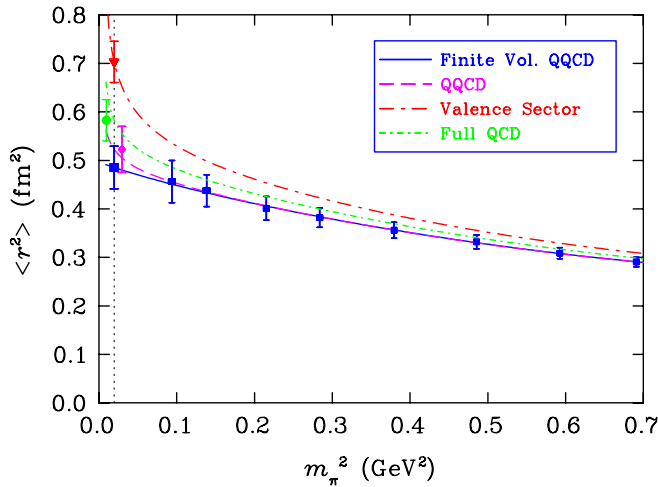


FIG. 6 (color online). The contribution of a single  $u$  quark with unit charge to the  $\Sigma^+$  charge radius versus pion mass. The square, rhombus, triangle, and round symbols are for the finite-volume quenched QCD, infinite volume quenched QCD, valence sector, and full-QCD results, respectively.

constituent-quark type expectation, and that the unusual chiral features are only anticipated to become dominant far below the physical quark mass.

We now discuss the quark distribution radius in strange octet baryons. The  $u$ -quark contribution to the  $\Sigma^+$  charge radius is shown in Fig. 6. In contrast to the proton case, in quenched QCD there is no pion-loop contribution to the  $\Sigma^+$  charge radius. The nontrivial loop contributions involve the  $K$  meson. Consequently, the  $u$ -quark distribution radius has no log divergence [as the  $SU(2)$  chiral limit is approached]. In full QCD, both the valence and total sectors exhibit log-divergent charge radii. At the physical

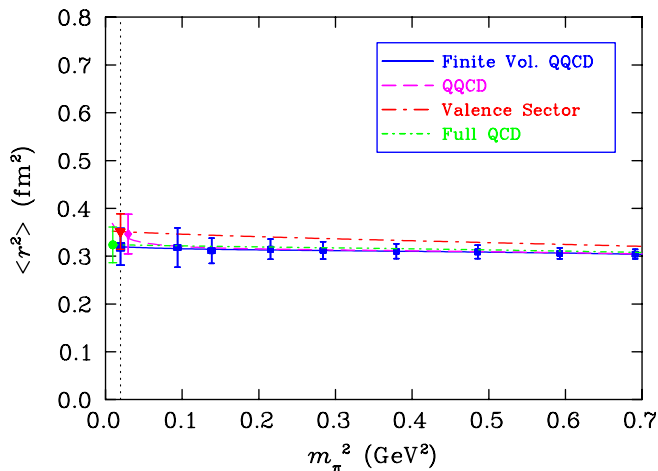


FIG. 7 (color online). The contribution of an  $s$  quark with unit charge to the  $\Sigma^+$  charge radius versus pion mass. The square, rhombus, triangle, and round symbols are for the finite-volume quenched QCD, infinite volume quenched QCD, valence sector, and full-QCD results, respectively.

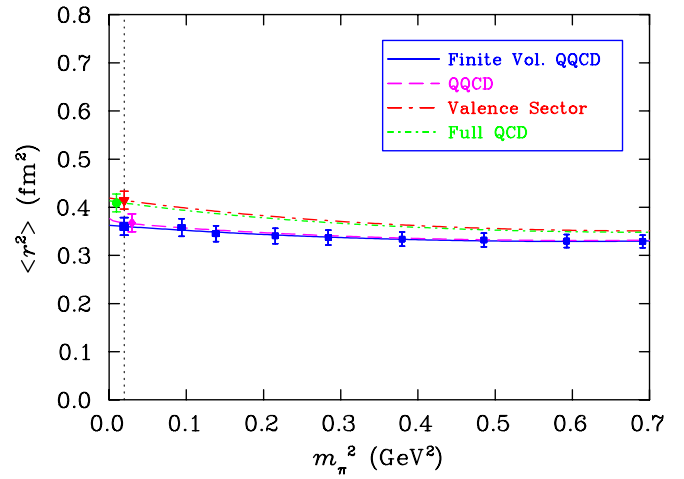


FIG. 8 (color online). The contribution of a single  $s$  quark with unit charge to the  $\Xi^0$  charge radius versus pion mass. The square, rhombus, triangle, and round symbols are for the finite-volume quenched QCD, infinite volume quenched QCD, valence sector, and full-QCD results, respectively.

pion mass, the total  $u$ -quark distribution radius is found to be very similar to that in the proton.

The singly represented quark of the  $\Sigma^+$  is a strange quark. We show its contribution to the  $\Sigma^+$  charge radius in Fig. 7. Since there cannot be any leading-order pion-loop contributions to the  $s$ -quark radius, the chiral corrections are much less dramatic than in the light-quark sector. One may also compare  $K$  contributions at the physical point with those of the light-quark sector as observed near  $m_\pi^2 \sim m_{K(\text{phys})}^2 \sim 0.25 \text{ GeV}^2$ . Because the  $s$  quark mass is held fixed, any variation is due to an environment effect associated with the light quarks.

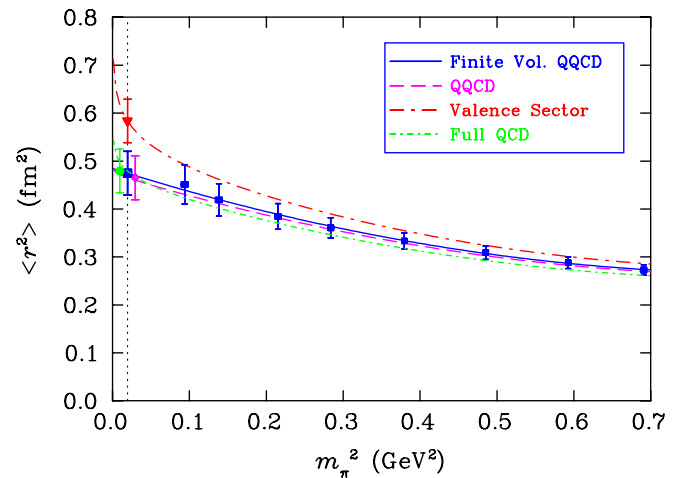


FIG. 9 (color online). The contribution of a  $u$  quark with unit charge to the  $\Xi^0$  charge radius versus pion mass. The square, rhombus, triangle, and round symbols are for the finite-volume quenched QCD, infinite volume quenched QCD, valence sector, and full-QCD results, respectively.

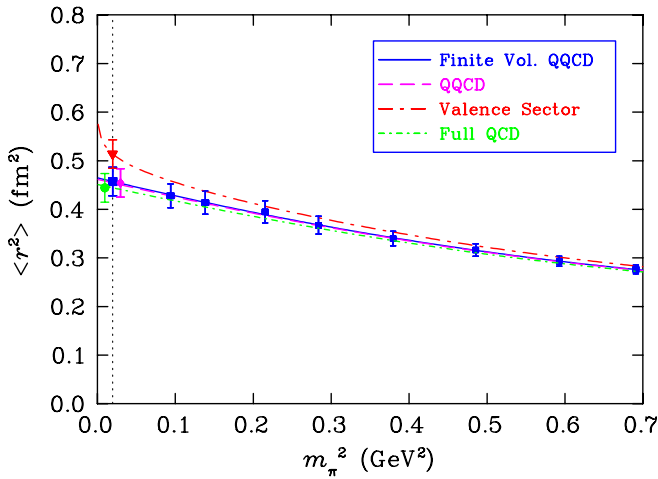


FIG. 10 (color online). The contribution of a single light quark with unit charge to the  $\Lambda$  charge radius versus pion mass. The square, rhombus, triangle, and round symbols are for the finite-volume quenched QCD, infinite volume quenched QCD, valence sector, and full-QCD results, respectively.

The  $\Xi^0$  is composed of two strange quarks and one up quark. The strange-quark contribution to  $\Xi^0$  is shown in Fig. 8. Similar to the  $s$  quark in the  $\Sigma^+$ , all the curves display a very mild environment dependence on the light-quark mass.

The  $u$ -quark contribution to the  $\Xi^0$  is shown in Fig. 9. In full QCD, both the full and valence contributions are divergent as  $m_\pi \rightarrow 0$ . Here, we see that the charge radius diverges in the positive direction, opposite to that of the  $d$  quark in the proton. Here, the pion loop must contain a light antiquark from the sea and thereby the valence  $u$  is pure quark (that is, it cannot be an antiquark, or it cannot couple to a pion through a  $Z$ -type diagram).

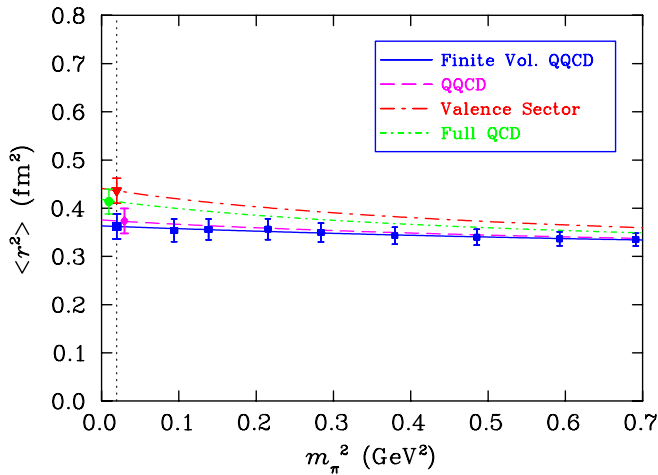


FIG. 11 (color online). The contribution of an  $s$  quark with unit charge to the  $\Lambda$  charge radius versus pion mass. The square, rhombus, triangle, and round symbols are for the finite-volume quenched QCD, infinite volume quenched QCD, valence sector and full-QCD results, respectively.

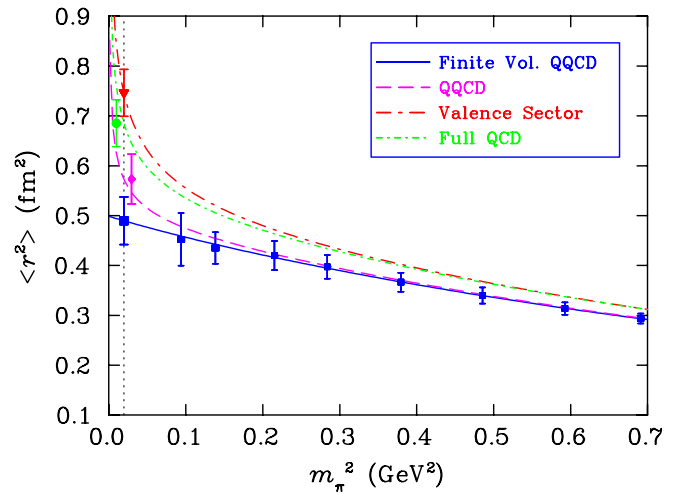


FIG. 12 (color online). The proton charge radius versus pion mass. The square, rhombus, triangle, and round symbols are for the finite-volume quenched QCD, infinite volume quenched QCD, valence sector, and full-QCD results, respectively.

The single light quark and strange-quark contribution to the  $\Lambda$  is shown in Figs. 10 and 11, respectively. It is interesting that the light quark sector does not show much curvature. This is consistent with the chiral coefficients for the leading-order pion dressing vanishing. The contribution from the  $\pi^+$  and  $\pi^-$  meson clouds cancel each other. The  $s$  quark in the  $\Lambda$  couples strongly to  $NK$ , and it looks like there is some environment dependence.

Using the charge-symmetry relations above, Eqs. (17)–(21), one can reconstruct any desired baryon form factors by applying the appropriate charge factors.

We now discuss the constructed octet-baryon charge radii. The proton charge radii are illustrated in Fig. 12.

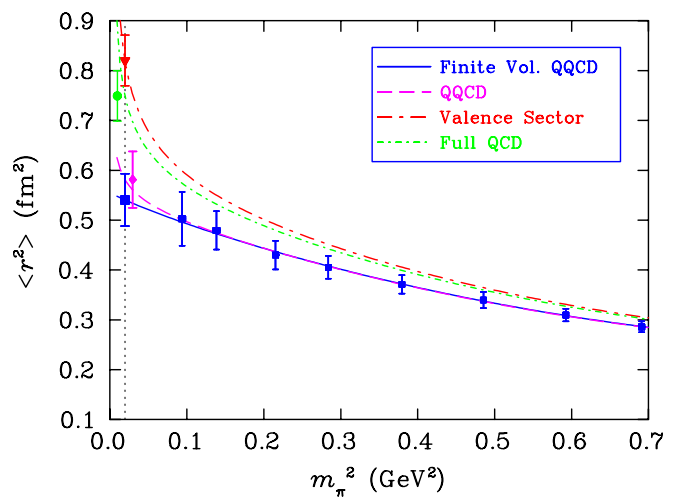


FIG. 13 (color online).  $\Sigma^+$  charge radius versus pion mass. The square, rhombus, triangle, and round symbols are for the finite-volume quenched QCD, infinite volume quenched QCD, valence sector, and full-QCD results, respectively.

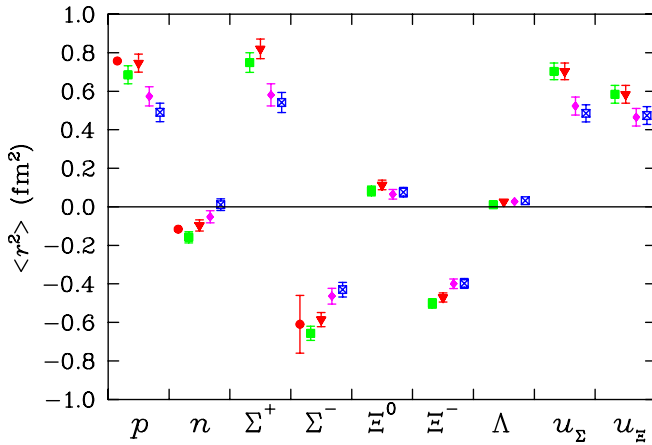


FIG. 14 (color online). Octet-baryon charge radii at the physical pion mass. The hollow square, solid rhombus, triangle, and square symbols are for the finite-volume quenched QCD, infinite volume quenched QCD, valence sector, and full-QCD results, respectively. The experimental data for proton, neutron, and  $\Sigma^-$  is shown with the left-most bullet.

At the physical pion mass, we find the proton charge radius is about  $0.69 \pm 0.05 \text{ fm}^2$ . The  $u$ ,  $d$ , and  $s$  quarks all provide a contribution to the proton charge radii. We note that the valence sector alone contributes a large fraction to the total charge radius. There is a small correction by adding all the disconnected contributions of the 3 light-quark flavors in the process of correcting QQCD via FRR EFT. Further, the strangeness component only constitutes a small part of this small correction [50].

The charge radius of  $\Sigma^+$  is shown in Fig. 13. The numerical value is observed to be a little larger than that of proton, with the physical charge radius of the  $\Sigma^+$  being  $0.75 \pm 0.05 \text{ fm}^2$ . The primary cause of this radius being larger than the proton is the fact that the (negatively charged) strange quark in the  $\Sigma$  has a narrower spatial distribution than the down quark in the proton.

In Fig. 14, the charge radii of the octet baryons at the physical pion mass are shown. The extrapolated physical

radii of the proton, neutron, and  $\Sigma^-$  are in good agreement with the experimental data. The radius of  $\Xi^0$  is positive, in contrast to the neutron radius. The reason is that, for the neutron, in full QCD, the  $\pi^-$  cloud is the dominant contribution, whereas for the  $\Xi^0$ , the pion intermediate state is a  $\pi^+$  (with a  $\Xi^-$  intermediate baryon). Since both  $\pi^+$  and  $\pi^-$  contribute to the  $\Lambda$ , the radius of the  $\Lambda$  is close to zero. This is perhaps surprising as one would expect the net positive charge of the light quarks to dominate more.

The results of our extrapolation and unquenching are summarized in Table IX. Here, we see a careful breakdown of the propagation of uncertainties at the various stages of calculation.

## V. SUMMARY

We extrapolated state-of-the-art lattice results for the quark-sector decomposition of the octet-baryon charge radii in quenched heavy-baryon chiral perturbation theory using FRR. All leading-loop diagrams have been incorporated, including all contributions from both octet and decuplet baryon intermediate states. Finite-range regularization has been utilized in the one-loop calculation to improve the convergence at moderate quark masses. Further, the use of FRR provides a separation of scales, which has enabled the use of a demonstrated technique to obtain estimates of the full-QCD results from the quenched lattice simulations. We acknowledge the phenomenological aspects of our calculation. As such, we have an empirically motivated extrapolation form, which is equivalent to the leading one-loop heavy baryon chiral perturbation theory form in the domain where higher-order terms are genuinely negligible.

The individual quark contributions to the baryon charge radii in quenched QCD have been extrapolated, with subsequent predictions for the corresponding radii in both valence and full QCD. We note that the valence predictions will be readily confronted with the next generation of lattice simulations of full QCD, as only connected current insertions are required. The contribution from pion loops is

TABLE IX. Summary of extrapolation and unquenching results. Each major column consists of our best value (in  $\text{fm}^2$ ), followed by the three dominant sources of uncertainty: statistical, lattice scale determination  $a = 0.128 \pm 0.006 \text{ fm}$  and regularization scale  $\Lambda = 0.8 \pm 0.1 \text{ GeV}$ , respectively, all quoted relative to the final digit of the best value. The sign of the uncertainty reflects the correlation with  $a$  or  $\Lambda$ .

	QQCD				Valence QCD				Total			Experiment	
$p$	0.573	50	45	8	0.746	47	42	27	0.685	47	42	21	$0.766 \pm 0.012$ [51]
$n$	-0.052	31	2	-5	-0.097	29	3	-9	-0.158	29	3	-15	$-0.1161 \pm 0.0022$ [51]
$\Sigma^+$	0.581	57	53	6	0.820	51	47	28	0.749	51	47	21	
$\Sigma^-$	-0.464	41	-42	-5	-0.586	37	-38	-17	-0.657	37	-38	-24	$-0.61 \pm 0.15$ [52]
$\Xi^0$	0.065	25	8	-1	0.113	25	8	4	0.082	25	8	-2	
$\Xi^-$	-0.400	25	-37	0	-0.471	24	-37	-12	-0.502	24	-37	-17	
$\Lambda$	0.027	8	3	0	0.026	8	3	-2	0.010	8	3	-4	
$u_\Sigma$	0.523	47	47	6	0.703	43	42	22	0.703	43	42	22	
$u_\Xi$	0.465	46	45	-1	0.584	46	45	16	0.584	46	45	16	

observed to generate significantly more enhancement of the radii than that from  $K$  mesons. Further, disconnected contributions to the radii are rather small compared with the dominant valence contributions. One of the consequences of this is that the strange-quark disconnected contributions only represent a small component of an already small correction.

The charge radii of the proton, neutron, and  $\Sigma^-$  are in good agreement with the experimental results. Our result for  $\Sigma^-$  is quite accurate relative to the current experimental measurement. Further, we have presented predictions for the remaining five baryons, for which no experimental information exists to date. These predictions remain to be

tested by potential future measurements and future studies in *ab initio* lattice QCD.

## ACKNOWLEDGMENTS

We thank the Australian Partnership for Advanced Computing (APAC) and eResearch South Australia for supercomputer support enabling this project. This work is supported by the Australian Research Council and by U.S. DOE Contract No. DE-AC05-06OR23177, under which Jefferson Science Associates, LLC operates Jefferson Laboratory, and Contract No. DE-AC02-06CH11357, under which UChicago Argonne, LLC operates Argonne National Laboratory.

- 
- [1] D. H. Lu, A. W. Thomas, and A. G. Williams, *Phys. Rev. C* **57**, 2628 (1998).
  - [2] K. Berger, R. F. Wagenbrunn, and W. Plessas, *Phys. Rev. D* **70**, 094027 (2004).
  - [3] B. Julia-Diaz, D. O. Riska, and F. Coester, *Phys. Rev. C* **69**, 035212 (2004); **75**, 069902(E) (2007).
  - [4] A. J. Buchmann and R. F. Lebed, *Phys. Rev. D* **67**, 016002 (2003).
  - [5] S. Cheedket, V. E. Lyubovitskij, T. Gutsche, A. Faessler, K. Pumsa-ard, and Y. Yan, *Eur. Phys. J. A* **20**, 317 (2004).
  - [6] R. A. Williams and C. Puckett-Truman, *Phys. Rev. C* **53**, 1580 (1996).
  - [7] G. Hellstern and C. Weiss, *Phys. Lett. B* **351**, 64 (1995).
  - [8] M. Oettel, G. Hellstern, R. Alkofer, and H. Reinhardt, *Phys. Rev. C* **58**, 2459 (1998).
  - [9] R. Alkofer, A. Holl, M. Kloker, A. Krassnigg, and C. D. Roberts, *Few-Body Syst.* **37**, 1 (2005).
  - [10] G. Eichmann, A. Krassnigg, M. Schwinzerl, and R. Alkofer, *Ann. Phys. (N.Y.)* **323**, 2505 (2008).
  - [11] S. J. Puglia, M. J. Ramsey-Musolf, and S. L. Zhu, *Phys. Rev. D* **63**, 034014 (2001).
  - [12] T. Fuchs, J. Gegelia, and S. Scherer, *J. Phys. G* **30**, 1407 (2004).
  - [13] B. Kubis and U. G. Meissner, *Eur. Phys. J. C* **18**, 747 (2001).
  - [14] B. Kubis and U. G. Meissner, *Nucl. Phys. A* **679**, 698 (2001).
  - [15] M. R. Schindler, J. Gegelia, and S. Scherer, *Eur. Phys. J. A* **26**, 1 (2005).
  - [16] J. M. Zanotti, D. B. Leinweber, A. G. Williams, and J. B. Zhang, *Nucl. Phys. B, Proc. Suppl.* **129**, 287 (2004).
  - [17] S. Boinepalli, D. B. Leinweber, A. G. Williams, J. M. Zanotti, and J. B. Zhang, *Phys. Rev. D* **74**, 093005 (2006).
  - [18] C. Alexandrou, G. Koutsou, J. W. Negele, and A. Tsapalis, *Phys. Rev. D* **74**, 034508 (2006).
  - [19] M. Gockeler *et al.* (QCDSF Collaboration), *Phys. Rev. D* **71**, 034508 (2005).
  - [20] M. Gockeler *et al.*, *Eur. Phys. J. A* **32**, 445 (2007).
  - [21] M. Gockeler *et al.* (QCDSF/UKQCD Collaboration), *Proc. Sci., LAT2007* (2007) 161.
  - [22] R. G. Edwards *et al.* (LHPC Collaboration), *Proc. Sci., LAT2005* (2006) 056.
  - [23] C. Alexandrou *et al.* (Lattice Hadron Physics Collaboration), *J. Phys. Conf. Ser.* **16**, 174 (2005).
  - [24] V. Bernard, *Prog. Part. Nucl. Phys.* **60**, 82 (2008).
  - [25] L. F. Li and H. Pagels, *Phys. Rev. Lett.* **26**, 1204 (1971).
  - [26] D. B. Leinweber and T. D. Cohen, *Phys. Rev. D* **47**, 2147 (1993).
  - [27] D. B. Leinweber, D. H. Lu, and A. W. Thomas, *Phys. Rev. D* **60**, 034014 (1999).
  - [28] D. B. Leinweber, A. W. Thomas, and R. D. Young, *Phys. Rev. Lett.* **86**, 5011 (2001).
  - [29] W. Detmold *et al.*, *Phys. Rev. Lett.* **87**, 172001 (2001).
  - [30] T. R. Hemmert and W. Weise, *Eur. Phys. J. A* **15**, 487 (2002).
  - [31] R. D. Young, D. B. Leinweber, and A. W. Thomas, *Prog. Part. Nucl. Phys.* **50**, 399 (2003).
  - [32] R. D. Young, D. B. Leinweber, and A. W. Thomas, *Phys. Rev. D* **71**, 014001 (2005).
  - [33] S. R. Beane, *Nucl. Phys. B* **695**, 192 (2004).
  - [34] D. Djukanovic, J. Gegelia, and S. Scherer, *Eur. Phys. J. A* **29**, 337 (2006).
  - [35] D. B. Leinweber, A. W. Thomas, and R. D. Young, *Phys. Rev. Lett.* **92**, 242002 (2004).
  - [36] J. Gasser and H. Leutwyler, *Nucl. Phys. B* **307**, 763 (1988).
  - [37] J. N. Labrenz and S. R. Sharpe, *Phys. Rev. D* **54**, 4595 (1996).
  - [38] M. J. Savage, *Nucl. Phys. A* **700**, 359 (2002).
  - [39] D. B. Leinweber, *Phys. Rev. D* **69**, 014005 (2004).
  - [40] D. Arndt and B. C. Tiburzi, *Phys. Rev. D* **68**, 094501 (2003).
  - [41] B. C. Tiburzi, *Phys. Rev. D* **71**, 054504 (2005).
  - [42] R. D. Young, D. B. Leinweber, A. W. Thomas, and S. V. Wright, *Phys. Rev. D* **66**, 094507 (2002).
  - [43] R. G. Edwards, U. M. Heller, and T. R. Klassen, *Nucl. Phys. B* **517**, 377 (1998).
  - [44] E. E. Jenkins and A. V. Manohar, *Phys. Lett. B* **255**, 558 (1991).
  - [45] V. Bernard, N. Kaiser, J. Kambor, and U. G. Meissner, *Nucl. Phys. B* **388**, 315 (1992).

- [46] V. Bernard, T.R. Hemmert, and U.G. Meissner, Nucl. Phys. **A732**, 149 (2004).
- [47] B. Kubis, T.R. Hemmert, and U.G. Meissner, Phys. Lett. B **456**, 240 (1999).
- [48] B. C. Tiburzi and A. Walker-Loud, Phys. Lett. B **669**, 246 (2008).
- [49] D. B. Leinweber *et al.*, Phys. Rev. Lett. **94**, 212001 (2005).
- [50] D. B. Leinweber *et al.*, Phys. Rev. Lett. **97**, 022001 (2006).
- [51] C. Amsler *et al.* (Particle Data Group), Phys. Lett. B **667**, 1 (2008).
- [52] I. M. Gough Eschrich *et al.* (SELEX Collaboration), Phys. Lett. B **522**, 233 (2001).